Geophysical Research Letters

RESEARCH LETTER
10.1029/2025GL115908

Imaging Brine Infiltration and Basal Marine Ice in Larsen C Ice Shelf, Antarctic Peninsula, From Borehole Measurements and Transient Electromagnetics

Siobhan F. Killingbeck[1], Bernd Kulessa[1,2], Katie E. Miles[3], Bryn Hubbard[4], Adrian Luckman[1], Sarah S. Thompson[5], Glenn Jones[1,6], and Benjamin K. Galton-Fenzi[5,7,8]

[1]Department of Geography, Faculty of Science and Engineering, Swansea University, Swansea, UK, [2]School of Geography, Planning, and Spatial Sciences, University of Tasmania, Hobart, TAS, Australia, [3]Lancaster Environment Centre, Faculty of Science and Technology, Lancaster University, Lancaster, UK, [4]Centre for Glaciology, Department of Geography and Earth Sciences, Aberystwyth University, Aberystwyth, UK, [5]Australian Antarctic Program Partnership, Institute of Marine and Antarctic Studies, University of Tasmania, Hobart, TAS, Australia, [6]School of Earth and Environmental Sciences, Cardiff University, Cardiff, UK, [7]Australian Antarctic Division, Kingston, TAS, Australia, [8]Australian Centre for Excellence in Antarctic Science at the University of Tasmania, Hobart, TAS, Australia

Key Points:

- TEM, ground-penetrating radar (GPR), seismic, and borehole data were used to image ice structure across the Joerg Peninsula suture zone
- GPR and borehole logs show a ~2.5 m thick brine-infiltrated layer at ~78 m depth, extending across the Larsen C suture zone
- TEM data suggest a conductive basal layer, consistent with porous (0.18–0.40) marine ice accreted beneath the ice shelf

Supporting Information:

Supporting Information may be found in the online version of this article.

Correspondence to:

S. F. Killingbeck,
s.f.killingbeck@swansea.ac.uk

Citation:

Killingbeck, S. F., Kulessa, B., Miles, K. E., Hubbard, B., Luckman, A., Thompson, S. S., et al. (2025). Imaging brine infiltration and basal marine ice in Larsen C Ice Shelf, Antarctic Peninsula, from borehole measurements and transient electromagnetics. *Geophysical Research Letters*, *52*, e2025GL115908. https://doi.org/10.1029/2025GL115908

Received 12 MAR 2025
Accepted 1 AUG 2025

Abstract The presence and nature of marine ice in ice shelves is important, yet difficult to determine. We present transient electromagnetic results spanning 10 km across a suture zone of Larsen C Ice Shelf (LCIS), Antarctica, supported by central borehole measurements. Our results indicate the presence of two ice-shelf layers. The uppermost layer, ~300 m thick, has resistivity 10^3–10^6 Ωm. We interpret this as meteoric ice, overlying a lower shelf layer 25–56 m thick with resistivity 3–20 Ωm, consistent with permeable basal marine ice. This reconstruction closely matches modeled marine-ice thicknesses in the area. The porosity of this layer is 0.18–0.40, higher than measured farther down-flow, suggesting the layer consolidates once formed. Within the upper layer at 78.5 m depth, we identify a 2.5 m thick layer, likely linked to brine infiltration. These heterogeneities in ice shelf properties should be accounted for in future LCIS stability assessments.

Plain Language Summary We used a novel method to image through the Larsen C Ice Shelf, Antarctica, at a suture zone, where two ice masses merge. We discovered two distinct layers: a 300-m-thick upper layer of dense, impermeable ice likely formed from compacted snow, and a thinner layer of porous, frozen seawater. The latter marine ice layer at the base of the ice shelf is less dense than that of a basal marine ice layer observed at a location 195 km downstream. This suggests the basal layer consolidates as it flows toward the ocean. Understanding this layered structure is essential for predicting the ice shelf's stability.

1. Introduction

Marine ice is important for many reasons including its role in the basal mass budget of ice shelves and its influence on shelf rheology and stability (Craw, 2023). Suture zones are present in all large and numerous smaller Antarctic ice shelves, stabilizing them by delaying the opening of rifts that propagate quickly through meteoric ice units derived from tributary glaciers (Jansen et al., 2015; Khazender et al., 2009; Kulessa et al., 2014, 2019). Basally accreted marine ice within suture zones contains seawater and is warmer than surrounding meteoric ice, allowing suture zones to arrest rifts by accommodating strain and delaying or preventing brittle fracture (Kulessa et al., 2019). For example, marine ice is well known to play a crucial role in stabilizing Larsen C Ice Shelf (LCIS), Antarctic Peninsula (Kulessa et al., 2014). However, a recent study by Harrison et al. (2022) shows that ocean warming significantly reduces the extent and thickness of LCIS' marine ice, with potential implications for the shelf's future stability.

Basal marine ice is formed through the accretion of seawater onto the ice shelf base and exhibits a heterogeneous structure. The structure consists of consolidated ice near the upper boundary where it merges with meteoric ice, often characterized by trapped salt within the ice matrix, and transitions to a less consolidated matrix at the lower interface (i.e., solid marine ice to permeable marine ice; Craven et al., 2009). This evolution is driven by the upward buoyancy of ice, basal refreezing induced by heat flux, and brine drainage, resulting in vertical gradients in temperature, salinity, and porosity (Galton-Fenzi et al., 2012).

The presence of basal marine ice can be inferred from joint consideration of digital elevation models, airborne radar data and hydrostatic equilibrium (Fricker et al., 2001; Holland et al., 2009), with processes of frazil ice accretion and compaction simulated by ocean models (Galton-Fenzi et al., 2012; Harrison et al., 2022). However, numerical simulations suffer from uncertainties in average ice-shelf densities that form the basis of ice-thickness calculations, in oceanographic conditions that control rates of basal freezing and melting, and in the actual process of formation and accretion of frazil ice at the base of the ice shelf. Furthermore, ice-shelf regions where basal undulations have spatial wavelengths smaller than the ice thickness may invalidate the hydrostatic floatation approximation (Stubblefield et al., 2023). These uncertainties are compounded in suture zones, whose internal ice composition is likely complex but usually poorly known (Kulessa et al., 2014, 2019; McGrath et al., 2014).

Radar attenuation is often used as an indirect indicator of marine ice due to its expected high electrical conductivity and scattering at the meteoric-marine ice interface (Kulessa et al., 2019). However, similar radar attenuation and diffuse scattering can also result from brine infiltration, an alternative process where seawater penetrates into near-surface or englacial layers. Brine infiltration has been observed on Antarctic ice shelves such as McMurdo, where seawater propagates laterally along structural boundaries or vertically through surface-connected fractures (Campbell et al., 2017; Kovacs & Gow, 1975). On the Brunt Ice Shelf, King et al. (2018) showed that strong radar scattering could be caused by brine-filled fractures rather than basal marine ice. This highlights the need to consider brine infiltration alongside basal marine ice formation when assessing ice-shelf internal structure from radar data.

To a certain extent, basal marine ice layers can be mapped and characterized physically using active-source seismic measurements (Kulessa et al., 2019; McMahon & Lackie, 2006), or borehole logging or sampling (Craven et al., 2005, 2009). However, seismic methods struggle to image the gradational transition from marine ice to ocean due to weak acoustic impedance contrasts (Brisbourne et al., 2020). Borehole logging and sampling can provide high resolution 1-D information about marine ice properties and ice crystal orientation fabrics, which directly control anisotropy, deformation, and ice flow, impacting ice shelf dynamics (Craven et al., 2009; Hubbard et al., 2012; Miles et al., 2025; Treverrow et al., 2010). Yet, these methods are spatially limited and logistically intensive. Consequently, there is an urgent need for measurements that are more feasibly acquired and not only capable of diagnosing the presence of basal marine ice, but also of characterizing its depth, thickness and physical properties such as porosity and seawater content.

Electromagnetic (EM) methods offer a promising alternative, capable of mapping bulk resistivity and porosity in ice-shelf settings. EM has been used to detect subglacial water beneath glaciers (Killingbeck et al., 2020; Mikucki et al., 2015) and to quantify sub-ice platelet layers (SIPLs) beneath sea ice (Brett et al., 2020; Haas et al., 2021; Hunkeler et al., 2016). Like SIPLs, basal marine ice is expected to exhibit intermediate resistivities, between resistive meteoric ice (>10,000 Ωm; Kulessa, 2007) and conductive seawater (∼0.36 Ωm; Nicholls et al., 2012), and its porosity can be estimated using empirical mixing models developed for sea ice (Gough et al., 2012; Haas et al., 2021; Langhorne et al., 2015). While crystal structure and formation timescales differ, these analogies support the use of EM to assess basal marine ice structure and porosity.

Here, we present the results of an integrated geophysical survey acquired in the 2022/23 austral summer on the Joerg Peninsula suture zone, LCIS (Figure 1). The survey, which aimed to investigate the thickness and electrical resistivity of the basal marine ice layer, combined surface-based transient electromagnetics (TEM), ground-penetrating radar (GPR) and active source seismics with borehole televiewer, sonic and electrical logs. Resistivity is used to infer the porosity and its spatial variability across the basal marine ice layer.

2. Methods

2.1. Transient Electromagnetics

TEM data were acquired with a Geonics PROTEM47 system consisting of a three-channel digital time-domain receiver unit, a three component multi-turn receiver coil (area 31.4 m^2), and a TEM47 battery-powered transmitter. A 4 × 100 m square transmitter loop was laid out and the receiver coil was placed in the center of the square. Twenty-one TEM soundings were acquired every 500 m along a 10 km long profile across the suture zone (Figure 1c). At each location the transmitter module was used to power 2 A of current around the 4 × 100 m square transmitter loop. A base frequency of 25 Hz was acquired with 30 measurement time gates, 30 s integration

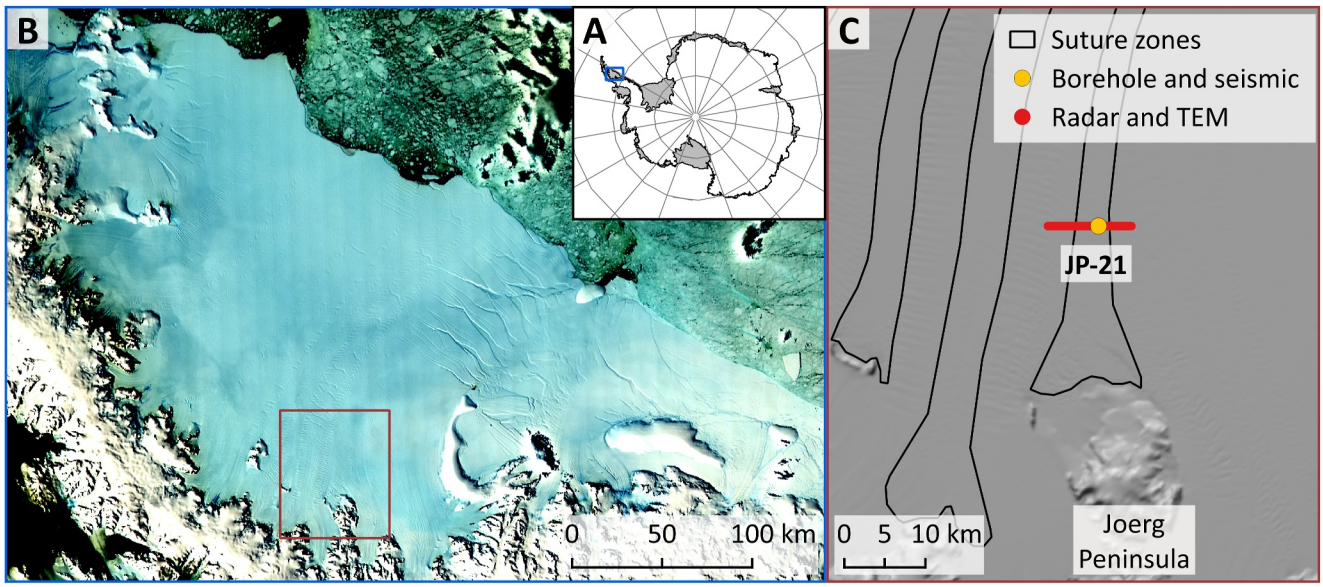

Figure 1. (a) Larsen C Ice Shelf, with location in Antarctica shown by blue rectangle in (b), and red rectangle indicating the field site in (c). The background is a MODIS scene from August 2016. (c) Joerg Peninsula suture zone with the location of the ground-penetrating radar survey line, TEM soundings, and JP-21, where the seismic and borehole data were acquired. The coastline and grounding line in (b) and background in (c) are from the MEaSUREs MODIS Antarctic mosaic (Haran et al., 2018). The coordinates of the start of the profile are −67.958191°, −64.432125°, and the end of the profile are −68.041545°, −64.325607°. The coordinates of the borehole location are −68.008614°, −64.367714°.

time, and seven stacks. Records of magnitude below background noise (measured at each site with the transmitter coil turned off) were rejected.

The positive TEM data for a normal decay curve were inverted to give an estimate of the resistivity and thickness of meteoric ice and basal marine ice. We applied the open-source MATLAB code MuLTI-TEM (S. Killingbeck, 2019, 2020) to invert the data using a trans-dimensional Bayesian inversion technique, which calculates the posterior probability density function of resistivity with respect to depth for each 1-D sounding (Killingbeck et al., 2020). This Bayesian inversion method typically selects a simple model, such as thick layers with minimal resistivity variations, unless additional geophysical data are provided as constraints. Therefore, we apply a constrained inversion, where the sub-shelf ocean halfspace is constrained at 0.36 Ωm, calculated from the CTD data acquired at the Southern site reported in Nicholls et al. (2012) with salinity 34.54 PSU, temperature −2.05°C, and pressure 30 Bars. The inversion parameters used in MuLTI-TEM are shown in Table S1 in Supporting Information S1.

The spatially variable porosities of the permeable basal marine ice layer are estimated from bulk electrical resistivity using Archie's Law (Archie, 1942). Archie's law is commonly used to derive the relationship between porosity and resistivity in porous sedimentary rocks, and should equally apply to SIPLs (Haas et al., 1997; Hunkeler et al., 2016) and glacier ice (Keller & Frischknecht, 1960; Killingbeck et al., 2022; Kulessa, 2007). Here, we use Archie's law to convert the estimated resistivity of the bulk permeable basal marine ice layer (R_m) to porosity (∅), as

$$\varnothing = \left(\frac{aR_s}{SR_m}\right)^{1/m} \quad (1)$$

where, R_s is the resistivity of the interstitial fluid in the permeable marine ice, set to the resistivity of seawater 0.36 Ωm (Nicholls et al., 2012), m is the cementation factor assumed to range between $m = 1.75$ (Haas et al., 1997) and $m = 3$ (Hunkeler et al., 2016), and the tortuosity factor (a) and saturation exponent (S) are set to 1 (e.g., Kovacs & Morey, 1986). It is noted that the resistivity of the interstitial fluid is unknown and could be lower than that of the underlying seawater. This is due to the exclusion of salts during ice formation, which concentrates them in the interstitial fluid, increasing its salinity and consequently lowering its resistivity.

2.2. Ground Penetrating Radar (GPR)

GPR data were acquired with a snow-scooter-towed assembly (Kulessa et al., 2019), using a Sensors and Software Pulse-Ekko Pro system with a 1000 V transmitter and 50 MHz dipole antennas mounted in perpendicular broadside mode on a plastic sledge, towed along a ∼10.6 km profile across the suture zone (Figure 1c). We acquired one trace every ∼2.5 m at a mean towing speed of ∼12 km hr^{-1}, representing a distance-averaged stack of eight individual traces at a sampling interval of 1.2 ns. Each stacked trace was located with a Leica GS10 GNSS rover, mounted on the snow scooter and post-processed in kinematic mode against a fixed base station operated on the ice shelf. Ground-penetrating radar data were imported into the commercial ReflexW software package and processed, including de-wow, bandpass filtering, and background noise removal. A velocity of 0.175 m ns^{-1}, derived previously from common-midpoint surveys in the same study area (Kulessa et al., 2014; Luckman et al., 2012), was used for depth conversion of the radargram. For this average velocity, the nominal wavelength of our 50 MHz GPR signal in ice is ∼3.5 m. With vertical resolution equal to around one-quarter wavelength, we expect to resolve layers thicker than ∼0.9 m near the ice-shelf surface. Resolution then becomes progressively worse with depth as higher radar frequencies are preferentially attenuated.

2.3. Active-Source Seismic

Active-source seismic data were acquired, with a spread of 48 vertical component geophones of 100 Hz with a sledgehammer impacting a thick plastic plate, at the borehole location near the center of the suture zone (Figure 1c). The geophones were placed at 2 m intervals, making the total spread length 94 m. Data were collected mid-way between individual geophones starting at off-end location −1 m and finishing at +95 m, thus totaling 49 shots along the spread. At least five hammer shots were stacked into a single gather for each shot point.

Seismic processing used MATLAB and the open-source CREWES package (Margrave et al., 2011). Traces next to each shot location were removed from the raw shot gathers thus removing over-saturated traces, and a bandpass filter was applied, with a 50–100 Hz low cut filter and 200–250 Hz high cut filter. The data were stacked to produce a common offset stack, with a maximum offset of 94 m. The P-wave velocity profile derived in Kulessa et al. (2019) was used to convert the seismic two-way-travel time (TWT) into depth.

2.4. Borehole Wireline Logging

A 120 m-deep borehole was drilled using hot-water and logged by optical televiewer (Miles et al., 2025), electric, and full waveform triple sonic probes from Robertson Geologging Ltd. The electric probe measures resistivity by producing a low-frequency bi-directional electric current from a source electrode on the probe, the return of which was measured by electrodes within the probe and converted to resistivity, relative to an earth stake submerged at the ice surface (∼5 m from the winch and ∼15 m from the borehole). Here, we report the long normal electrode resistivity. The full waveform triple sonic probe emits a high-frequency acoustic wave from a piezoelectric transmitter housed within the probe. The first arrival transit time was detected at three receivers within the probe and converted to sonic velocity based on the distance between the receivers in conjunction with an accurate quartz clock. Both the electric and sonic logs were acquired during up-logging (i.e., while the probes were being raised up the borehole).

3. Results

Outside the suture zone, the GPR data are characterized by multiple diffraction hyperbolas from the base of the ice shelf at depths between ∼300 and ∼350 m (Figure 2b). At the 10 km position, a basal crevasse is observed extending upwards to 200 m depth. Comparing the depth of the hyperbolas' apexes in the radargram with the ice thicknesses derived from BedMachine v3 (Morlighem et al., 2020), we find that the latter underestimates the ice thickness along this line by up to ∼50 m (Figure 2a). Inside the suture zone, the GPR data are characterized by multiple shallow diffraction hyperbolas at an average depth of ∼78 m (Figure 3a), and the base of the ice shelf is not visible. The borehole resistivity log is marked by a decrease from 9,500 Ωm to 8,000 Ωm through this shallow layer (Figure 3d).

A three-layer model fits the data best in our constrained TEM inversions, with the upper layer characterized by resistivities ranging between 1,000 Ωm and 1,000,000 Ωm (Figure 2b; Figure S1 in Supporting Information S1). This range encompasses the values measured by our borehole resistivity log (Figure 3c), although the inverted

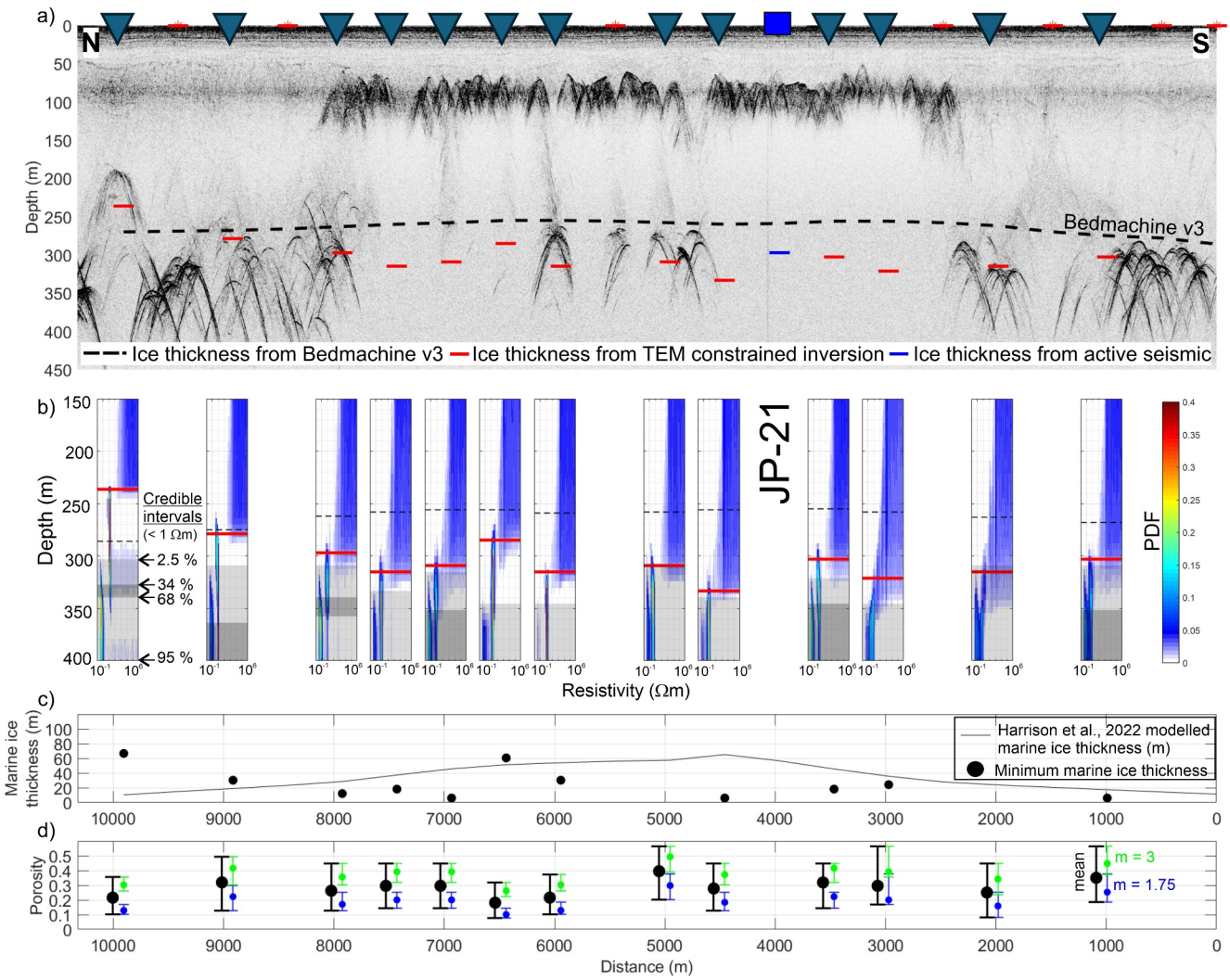

Figure 2. (a) Processed radargram (showing the magnitude of the analytic signal, derived from the Hilbert transform, which represents the envelope) with TEM station locations shown by the blue triangles. (b) Constrained TEM inversion results. (c) Estimated minimum thickness of basal marine ice along the radar line. (d) Estimated porosity of the basal marine ice layer along the radar line, green error bars are porosities derived with $m = 3$, blue error bars are porosities derived with $m = 1.75$ and black error bars are the mean. In (a and b), the depth of the resistive upper layer, picked from the TEM, is highlighted by the red lines. The black dotted line is the ice thickness derived from BedMachine v3. In (a), the depth of the observed seismic reflection (Figure 3b) is highlighted by the blue line. In (b), the estimated depth of the transition to seawater is highlighted by the gray box.

TEM data do not resolve the resistivity decrease (from 9,500 Ωm to 8,000 Ωm) shown at ~78 m depth. We pick the depth of the upper layer when the 50% credible interval is less than 1,000 Ωm. The average depth across the profile is 300 ± 10 m excluding the TEM measurement over the basal crevasse at the 10 km position (Figure 2b). The picked depths of the upper layer match closely those of the diffraction hyperbolas in the radargram at the base of the ice shelf (Figure 2a). Beneath this resistive upper layer, we detect an intermediate conductor characterized by resistivities of 3–20 Ωm (Figure 2b). The data points associated with the base of this intermediate conductor are close to levels of background noise (Figure S1 in Supporting Information S1), thus making it difficult to pick an exact depth to the lower layer. Therefore, a depth range is determined when the 2.5% credible interval (2 standard deviations) and 34% credible interval (one standard deviation) is less than 1 Ωm (Figure 2b). The minimum thickness of the intermediate conductor is estimated by subtracting the depth of the upper layer from the depth at which the 2.5% credible interval is less than 1 Ωm (Figure 2c). In all soundings the minimum thickness is greater than 0 m, highlighting the resistivity of the intermediate layer has a unique solution. Finally, the lowermost layer is the constrained seawater halfspace (0.36 Ωm).

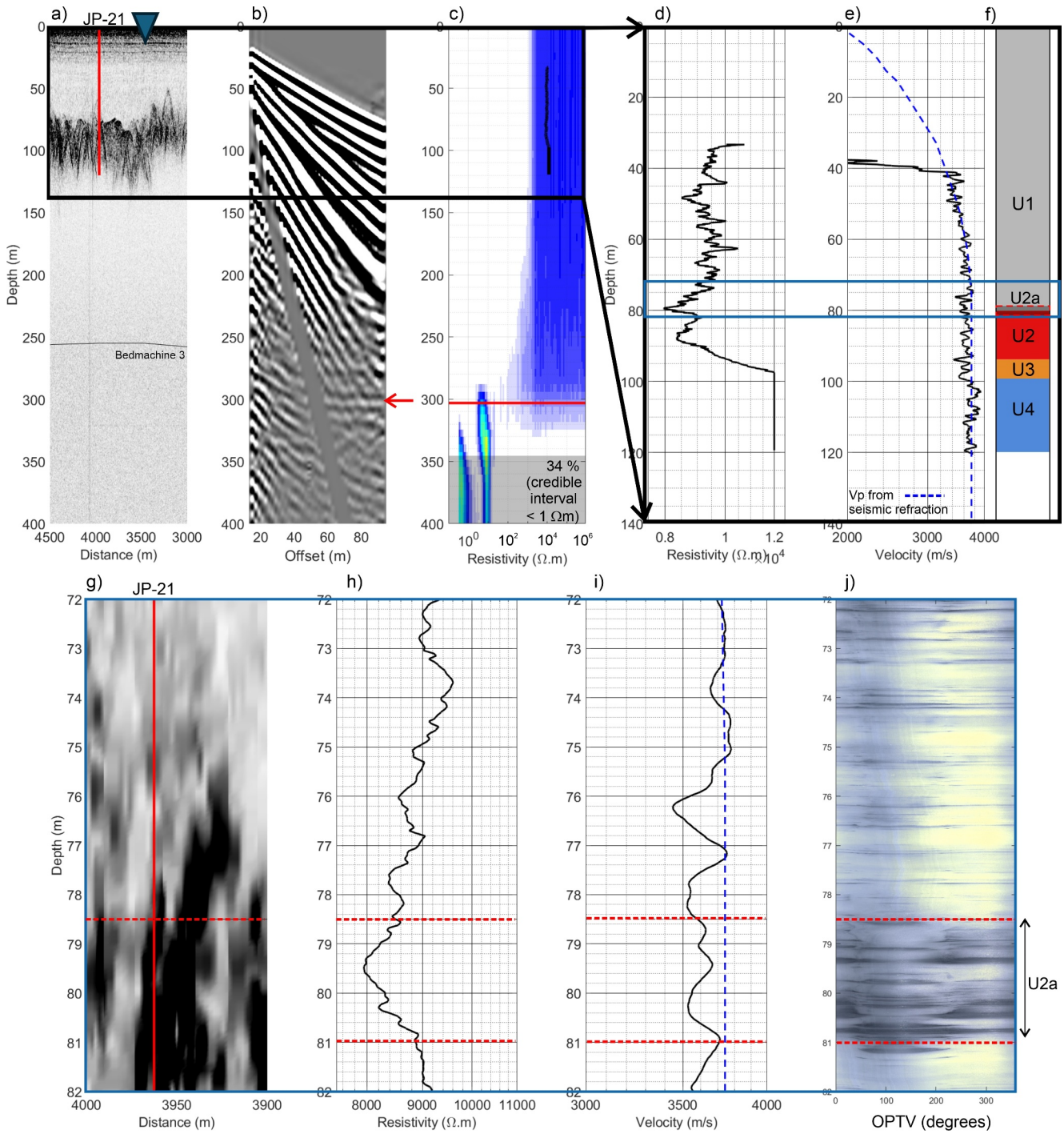

Figure 3. (a) Zoomed in section around JP-21 of the processed radargram, showing the envelope. (b) Seismic common offset stacked data in depth. The red arrow highlights the observed negative polarity reflection (black-white-black), where the polarity of the direct wave (defining a positive polarity) is white-black-white. (c) Constrained TEM inversion result of the sounding next to JP-21 with the electrical resistivity log plotted (black line). (d) Electrical resistivity log. (e) Sonic log (black line) and *Vp* profile derived in Kulessa et al., 2019 (blue dashed line). (f) Optical televiewer (OPTV) interpreted units 1–4 (U1–U4), plotted adjacent to the borehole wireline logs, reported in Miles et al., 2025, and U2a picked in this study. (g) Zoomed in section of the processed radargram between 72 and 82 m.(h) Zoomed in section of the resistivity log between 72 and 82 m. (i) Zoomed in section of the sonic log between 72 and 82 m. (j) OPTV log with Unit 2a.

The common-offset stacked seismic data indicate a weak negative reflector (black-white-black) at a TWT of 0.167 s (Figure 3b). The P-wave velocity profile derived in Kulessa et al. (2019) agrees closely with the borehole sonic log (Figure 3e) and is used to convert the TWT of the common offset stack to depth, where the weak

negative reflector occurs at a depth of ∼300 m (Figure 3b). This depth matches closely with that of the resistive upper layer picked from the TEM constrained inversions (∼303 m) next to JP-21 (Figure 3c).

4. Discussion

4.1. Properties of the Basal Marine Ice Layer

The GPR, TEM and seismic data are all consistent with the presence of an interface at ∼300 m depth. This interface is characterized by a large decrease in resistivity (from ∼1,000–∼1,000,000 Ωm to 3–20 Ωm) and a decrease in acoustic impedance as indicated by the negative polarity wavelet of seismic basal reflection. We interpret this interface to be a transition from meteoric ice, or potentially impermeable marine ice (Craven et al., 2009) with electrical properties in the range 1,000–1,000,000 Ωm, to permeable basal marine ice that corresponds to the intermediate conductor delineated by the inversion results (Figure 2b). The TEM-derived basal marine ice thicknesses are on the same order of magnitude as those modeled by Harrison et al. (2022) (Figure 2c), except in the presence of basal crevasses where they differ significantly (e.g., at the 10 km position of the GPR line the difference is ∼80 m; Figures 2a and 2c) highlighting the importance of field measurements.

The resistivity values of the basal marine ice layer are picked from the TEM data and converted to porosity using Equation 1. The mean estimated porosities along the profile range from 0.18 to 0.40 (Figure 2d). Acknowledging that the interstitial fluid resistivity (R_s) could be lower than the seawater resistivity used in our porosity calculations (Equation 1), and that the temperature may deviate from the assumed −2.05°C, we performed a sensitivity analysis. Utilizing temperature data from JP-21, extrapolated to 300 m depth, we estimated an upper temperature bound of 0°C (Figure S2a in Supporting Information S1) for this analysis. Systematically varying the temperature from −2.05°C to 0°C resulted in a negligible impact the calculated porosity range (Figure S2b in Supporting Information S1). Similarly, we estimate the upper R_s bound using a salinity of 120 psu, when solid precipitates start to form in seawater changing its composition (Sharqawy et al., 2010), yielding an R_s of 0.12 Ωm. By systematically varying R_s from 0.12 to 0.45 Ωm (Figure S2c in Supporting Information S1), the analysis demonstrates that our reported range sufficiently accounts for variations in R_s. Notably, a minimum R_s of 0.12 Ωm, would yield a lower mean porosity range of 0.12–0.25 (Figure S2c in Supporting Information S1), similar to the 0.14–0.20 range estimated at the Amery Ice Shelf (Craven et al., 2009). However, this high salinity is only likely in a brine drainage scenario near the upper part of the marine ice matrix and not representative of the bulk marine ice properties.

Our calculated porosity range (0.18–0.40) is notably higher than that (0.02–0.13) reported for a site located 195 km downflow (Kulessa et al., 2019) (Figure S3 in Supporting Information S1), suggesting that basal marine ice compacts as it travels along the suture zone (Figure S3b in Supporting Information S1). Compaction reduces both the overall thickness and the seawater content of the basal marine ice, which exerts the strongest control on its ability to arrest rifts (Kulessa et al., 2019). This ability is therefore likely largest at an unknown intermediate location along the suture zone where basal marine ice thickness and seawater content reach a maximum, relative to the thickness of meteoric ice prone to brittle fracture. That ability will then decrease toward the calving front as the marine ice progressively compacts, which may have implications for the future stability of the LCIS if basal melting increases in a warming sub-shelf ocean cavity (Kulessa et al., 2014; McGrath et al., 2014).

4.2. Properties of Suture Zone Internal Ice Shelf Units

Given a nominal vertical resolution of our 50 MHz GPR data of ∼1 m at 78.5 m depth, the 2.5 m thick Unit 2a should readily be detectable. Indeed, inside the suture zone at an average depth of ∼78 m, the GPR data are consistently characterized by multiple diffraction hyperbolas. The notable resistivity decrease at that depth in our wireline log (Figure 3h, from 9,500 Ωm to 8,000 Ωm) is not however sensed by TEM because the method is only sensitive to changes in resistivity when the bulk resistivity is <∼1,000 Ωm.

However, here we use the wireline resistivity and sonic logs to derive properties of the interface imaged in the GPR data and other internal ice shelf units reported in Miles et al. (2025). Figure 3f shows four internal ice shelf units interpreted from OPTV logs in Miles et al. (2025): Unit 1 is ice-shelf accumulated ice, Unit 2 is ice accumulated during transport over the grounding zone that is heavily deformed and fractured, Unit 3 is meteoric ice with shallow layer dips, and Unit 4 is meteoric ice with high layer dips. Here, we pick Unit 2a at 78.5 m depth characterized by a change in dielectric permittivity (Figure 3g), a decrease in resistivity from 9,355 Ωm to

8,230 Ωm (Figure 3h; Table S2 in Supporting Information S1), a decrease in sonic velocity from 3,673 m/s to 3,595 m/s (Figure 3i; Table S2 in Supporting Information S1) and dark layers in the OPTV log interpreted as bubble-free ice (Figure 3j). Borehole temperature measurements in JP-21 indicate that the temperature of Unit 2a is −5.8°C (Figure S2 in Supporting Information S1).

In the absence of a viable alternative explanation, we propose the change in geophysical properties at 78.5 m depth is likely caused by brine intrusion. Brine intrusion would cause local melting and refreezing of the surrounding ice to form the darker layers identified in Figure 3j. The salinity of brine at −5.8°C is ∼95 PSU (Figure S4a in Supporting Information S1), calculated using the UNESCO equation (Fofonoff & Millard, 1983), therefore $R_s = 0.17$ Ωm, calculated using the practical salinity scale (Perkin & Lewis, 1980). With a PSU of ∼95, the brine is therefore nearly three times as concentrated as seawater (35 PSU). This inference is consistent with significant refreezing of the pore space since brine intrusion took place, and therefore the genesis of the bubble-free dark layers in Unit 2a in the OPTV log (Figure 3j). Using Equation 1, the porosity of Unit 2a is estimated between 0.002 and 0.027, with $m = 1.75$ and $m = 3$.

We suggest that brine infiltration into Unit 2a occurred via a hybrid mechanism combining aspects of surface-driven firn loading and lateral intrusion along structural weaknesses. The configuration illustrated by King et al. (2018), see Figure 8 and 9 in King et al., 2018, provides a compelling model: sea ice forms in narrow channels between icebergs emerging from meteoric ice flowing to a grounding zone from a bedrock trough, and subsequent firn accumulation depresses this sea ice below sea level, allowing seawater to infiltrate the overlying permeable firn from below (King et al., 2018). In our case, however, the brine signal is more diffuse and radar-scattering, characterized by numerous hyperbolas, rather than a sharp interface as seen in McMurdo Ice Shelf brine studies (e.g., Campbell et al., 2017). This suggests multiple point-source intrusions rather than a single continuous brine horizon. We hypothesize that seawater infiltrated laterally along the top of impermeable ice within the suture zone, exploiting tensile fractures that formed as heavily deformed ice (Unit 2) was advected over the grounding zone. This deformed ice unit, documented in recent work by Miles et al. (2025), may have facilitated episodic brine infiltration that has since partially refrozen, consistent with our geophysical evidence and the formation of bubble-free dark layers observed in the OPTV logs.

5. Conclusions

Our study demonstrates the value of TEM methods for detecting and characterizing permeable basal marine ice in suture zones, including quantifying meteoric ice thickness and estimating the resistivity and porosity of basal marine ice where conventional geophysical approaches often fail. We observe a 300 ± 10 m thick, resistive (1,000–1,000,000 Ωm) meteoric ice layer, potentially including solid marine ice, overlying a conductive (3–20 Ωm) basal layer interpreted as porous marine ice, with estimated porosities between 0.18 and 0.40. These porosities are notably higher than the 0.02–0.13 estimated by Kulessa et al. (2019), at a location downflow along the same suture zone, indicating potential basal marine ice compaction along the suture zone. Thus, suggesting a possible weakening of the LCIS's buttressing capacity.

In addition, we identify a thin (∼2.5 m), laterally extensive brine-infiltrated layer at ∼78.5–81 m depth within the suture zone. This layer exhibits porosities between 0.002 and 0.027 and is likely associated with brine infiltration through surface-connected fractures, followed by localized melting and refreezing. The presence of this layer emphasizes that brine infiltration processes generate radar scattering signatures similar to those attributed to marine ice and thus must be accounted for in interpretations of radar or other remote sensing data sets.

These findings underscore the internal heterogeneity of ice shelves and the need for integrated geophysical approaches that distinguish between basal marine ice accretion and brine infiltration when evaluating ice shelf structure, mechanical integrity, and vulnerability to climate-driven change.

Data Availability Statement

All data presented in this paper are available through the UK Polar Data Centre. The borehole electric log is available at Hubbard et al. (2024c). The borehole sonic log is available at Hubbard et al. (2024b). The temperature profile is available at Hubbard et al. (2024a). The TEM data is available at Kulessa, Thompson, et al. (2025). The

seismic data is available at Kulessa, Miles, et al. (2025). The GPR data is available at Kulessa and Miles (2025). The MuLTI_TEM inversion algorithm is available at S. Killingbeck (2019).

Acknowledgments
This research is part of the NERC-funded RiPIce (Rift Propagation for Ice sheet models) research project, NERC standard Grant NE/T008016/1. We thank the British Antarctic Survey for logistical support, particularly the project's Field Guides: Samuel Hunt, Sarah Crowsley, and Min Willis.

References

Archie, G. E. (1942). The electrical resistivity log as an aid in determining some reservoir characteristics. *Transactions of the AIME*, *146*(1), 54–62. https://doi.org/10.2118/942054-g

Brett, G. M., Irvin, A., Rack, W., Haas, C., Langhorne, P. J., & Leonard, G. H. (2020). Variability in the distribution of fast ice and the sub-ice platelet layer near McMurdo iIce Shelf. *J. Geophys. Res.-Oceans*, *125*(3), e2019JC015678. https://doi.org/10.1029/2019JC015678

Brisbourne, A., Kulessa, B., Hudson, T., Harrison, L., Holland, P., Luckman, A., et al. (2020). An updated seabed bathymetry beneath Larsen C ice shelf, Antarctic Peninsula. *Earth System Science Data*, *12*(2), 887–896. https://doi.org/10.5194/essd-12-887-2020

Campbell, S., Courville, Z. R., Sinclair, S. N., & Wilner, J. (2017). *Geophysical survey of McMurdo Ice Shelf to determine infrastructure stability and future planning*. US Army Engineer Research and Development Center, Cold Regions Research and Engineering Laboratory.

Craven, M., Allison, I., Fricker, H. A., & Warner, R. (2009). Properties of a marine ice layer under the Amery Ice Shelf, East Antarctica. *Journal of Glaciology*, *55*(192), 717–728. https://doi.org/10.3189/002214309789470941

Craven, M., Carsey, F., Behar, A., Matthews, J., Brand, R., Elcheikh, A., et al. (2005). Borehole imagery of meteoric and marine ice layers in the Amery Ice Shelf, East Antarctica. *Journal of Glaciology*, *51*(172), 75–84. https://doi.org/10.3189/172756505781829511

Craw, L. (2023). *The influence of marine ice on ice shelf dynamics and stability*. Thesis. University of Tasmania.

Fofonoff, P., & Millard, R. C. Jr. (1983). Algorithms for computation of fundamental properties of seawater. In *UNESCO technical papers in marine science* (Vol. 44, p.53).

Fricker, H. A., Popov, S., Allison, I., & Young, N. (2001). Distribution of marine ice beneath the Amery Ice Shelf. *Geophysical Research Letters*, *28*(11), 2241–2244. https://doi.org/10.1029/2000GL012461

Galton-Fenzi, B. K., Hunter, J. R., Coleman, R., Marsland, S. J., & Warner, R. C. (2012). Modeling the basal melting and marine ice accretion of the Amery Ice Shelf. *Journal of Geophysical Research*, *117*(C9), C09031. https://doi.org/10.1029/2012JC008214

Gough, A. J., Mahoney, A. R., Langhorne, P. J., Williams, M. J. M., & Haskell, T. G. (2012). Sea ice salinity and structure: A winter time series of salinity and its distribution. *Journal of Geophysical Research*, *117*(C3), C03008. https://doi.org/10.1029/2011JC007527

Haas, C., Gerland, S., Eicken, H., & Miller, H. (1997). Comparison of sea-ice thickness measurements under summer and winter conditions in the Arctic using a small electromagnetic induction device. *Geophysical Research Letters*, *62*(3), 749–757. https://doi.org/10.1190/1.1444184

Haas, C., Langhorne, P. J., Rack, W., Leonard, G. H., Brett, G. M., Price, D., et al. (2021). Airborne mapping of the sub-ice platelet layer under fast ice in McMurdo Sound, Antarctica. *The Cryosphere*, *2020*, 1–31. https://doi.org/10.5194/tc-15-247-2021

Haran, T., Klinger, M., Fahnestock, M., Painter, T., & Scambos, T. (2018). *MEaSUREs MODIS mosaic of Antarctica 2013-2014 (MOA2014) image map, version 1*. NASA National Snow and Ice Data Center Distributed Active Archive Center. https://doi.org/10.5067/RNF17BP824UM

Harrison, L. C., Holland, P. R., Heywood, K. J., Nicholls, K. W., & Brisbourne, A. M. (2022). Sensitivity of melting, freezing and marine ice beneath Larsen C Ice Shelf to changes in ocean forcing. *Geophysical Research Letters*, *49*(4), e2021GL096914. https://doi.org/10.1029/2021GL096914

Holland, P. R., Corr, H. F., Vaughan, D. G., Jenkins, A., & Skvarca, P. (2009). Marine ice in Larsen ice shelf. *Geophysical Research Letters*, *36*(11), L11604. https://doi.org/10.1029/2009GL038162

Hubbard, B., & Miles, K., & RiPIce Project Team. (2024a). Ice temperature time-series from the southern sector of Larsen C Ice Shelf, Antarctic Peninsula, November-December 2022 (version 1.0) [Dataset]. *NERC EDS UK Polar Data Centre*. https://doi.org/10.5285/b2faed8b-ed62-44c2-b127-994deb548a41

Hubbard, B., & Miles, K., & RiPIce Project Team. (2024b). Borehole sonic log from the southern sector of Larsen C Ice Shelf, Antarctic Peninsula, December 2022 (version 1.0) [Dataset]. *NERC EDS UK Polar Data Centre*. https://doi.org/10.5285/6cc129aa-5dae-4c3c-a471-4974c2bcb8bf

Hubbard, B., & Miles, K., & RiPIce Project Team. (2024c). Borehole electric log from the southern sector of Larsen C Ice Shelf, Antarctic Peninsula, December 2022 (version 1.0) [Dataset]. *NERC EDS UK Polar Data Centre*. https://doi.org/10.5285/f7d8439f-eea3-4edb-be2e-99b290a82f06

Hubbard, B., Tison, J. L., Pattyn, F., Dierckx, M., Boereboom, T., & Samyn, D. (2012). Optical-televiewer-based identification and characterization of material facies associated with an Antarctic ice-shelf rift. *Annals of Glaciology*, *53*(60), 137–146. https://doi.org/10.3189/2012AoG60A045

Hunkeler, P. A., Hoppmann, M., Hendricks, S., Kalscheuer, T., & Gerdes, R. (2016). A glimpse beneath Antarctic sea ice: Platelet layer volume from multifrequency electromagnetic induction sounding. *Geophysical Research Letters*, *43*(1), 222–231. https://doi.org/10.1002/2015GL065074

Jansen, D., Luckman, A. J., Cook, A., Bevan, S., Kulessa, B., Hubbard, B., & Holland, P. R. (2015). Brief communication: Newly developing rift in Larsen C Ice Shelf presents significant risk to stability. *The Cryosphere*, *9*(3), 1223–1227. https://doi.org/10.5194/tc-9-1223-2015

Keller, G. V., & Frischknecht, F. C. (1960). Electrical resistivity studies on the Athabasca glacier, Alberta, Canada. *Journal of Research of the National Bureau of Standards D*, *64*(5), 439–448. https://doi.org/10.6028/jres.064d.053

Khazendar, A., Rignot, E., & Larour, E. (2009). Roles of marine ice, rheology, and fracture in the flow and stability of the Brunt/Stancomb-Wills Ice Shelf. *Journal of Geophysical Research*, *114*(4), 1–9. https://doi.org/10.1029/2008JF001124

Killingbeck, S. (2019). eespr/MuLTI-TEM: Multi-tem all ground-based surveys (MuLTI-TEM) [Software]. *Zenodo*. https://doi.org/10.5281/zenodo.3471639

Killingbeck, S. F., Booth, A. D., Livermore, P. W., Bates, C. R., & West, L. J. (2020). Characterisation of subglacial water using a constrained transdimensional Bayesian transient electromagnetic inversion. *Solid Earth*, *11*(1), 75–94. https://doi.org/10.5194/se-11-75-2020

Killingbeck, S. F., Dow, C. F., & Unsworth, M. J. (2022). A quantitative method for deriving salinity of subglacial water using ground-based transient electromagnetics. *Journal of Glaciology*, *68*(268), 319–336. https://doi.org/10.1017/jog.2021.94

King, E. C., De Rydt, J., & Gudmundsson, G. H. (2018). The internal structure of the Brunt Ice Shelf from ice-penetrating radar analysis and implications for ice shelf fracture. *The Cryosphere*, *12*(10), 3361–3372. https://doi.org/10.5194/tc-12-3361-2018

Kovacs, A., & Gow, A. J. (1975). Brine infiltration in the McMurdo Ice Shelf, McMurdo Sound, Antarctica. *Journal of Geophysical Research*, *80*(15), 1957–1961. https://doi.org/10.1029/JC080i015p01957

Kovacs, A., & Morey, R. M. (1986). Electromagnetic measurements of multi-year sea ice using impulse radar. *Cold Regions Science and Technology*, *12*(1), 67–93. https://doi.org/10.1016/0165-232x(86)90021-2

Kulessa, B. (2007). A critical review of the low-frequency electrical properties of ice sheets and glaciers. *Journal of Environmental and Engineering Geophysics*, *12*(1), 23–36. https://doi.org/10.2113/JEEG12.1.23

Kulessa, B., Booth, A. D., O'Leary, M., McGrath, D., King, E. C., Luckman, A. J., et al. (2019). Seawater softening of suture zones inhibits fracture propagation in Antarctic ice shelves. *Nature Communications*, *10*(1), 5491. https://doi.org/10.1038/s41467-019-13539-x

Kulessa, B., Jansen, D., Luckman, A. J., King, E. C., & Sammonds, P. R. (2014). Marine ice regulates the future stability of a large Antarctic ice shelf. *Nature Communications*, *5*(1), 3707. https://doi.org/10.1038/ncomms4707

Kulessa, B., & Miles, K. (2025). Ground-penetrating radar data from the southern sector of Larsen C Ice Shelf, Antarctic Peninsula, 2022 (version 1.0) [Dataset]. *NERC EDS UK Polar Data Centre*. https://doi.org/10.5285/9c46ec89-e2da-4140-a8a5-443911fe34cc

Kulessa, B., Miles, K., Luckman, A., & Hubbard, B. (2025a). Active source seismic survey from the southern sector of Larsen C Ice Shelf, Antarctic Peninsula, December 2022 (version 1.0) [Dataset]. *NERC EDS UK Polar Data Centre*. https://doi.org/10.5285/847a2898-51d1-4b74-a7b5-c73f179c8943

Kulessa, B., Thompson, S., Miles, K., Luckman, A., & Hubbard, B. (2025b). Transient electromagnetic survey from the southern sector of Larsen C Ice Shelf, Antarctic Peninsula, December 2022 (version 1.0) [Dataset]. *NERC EDS UK Polar Data Centre*. https://doi.org/10.5285/873edd47-f5c2-47cb-bf0c-3f45232536ca

Langhorne, P. J., Hughes, K. G., Gough, A. J., Smith, I. J., Williams, M. J. M., Robinson, N. J., et al. (2015). Observed platelet ice distributions in Antarctic sea ice: An index for ocean-ice shelf heat flux. *Geophysical Research Letters*, *42*(13), 5442–5451. https://doi.org/10.1002/2015GL064508

Luckman, A., Jansen, D., Kulessa, B., King, E. C., Sammonds, P., & Benn, D. I. (2012). Basal crevasses in Larsen C Ice Shelf and implications for their global abundance. *The Cryosphere*, *6*(1), 113–123. https://doi.org/10.5194/tc-6-113-2012

Margrave, G. F., Lamoureux, M. P., & Henley, D. C. (2011). The CREWES MATLAB toolbox: Seismic exploration and processing tools [Software]. *The CREWES Project, University of Calgary*. Reterived from https://www.crewes.org/ResearchLinks/FreeSoftware/index.php

McGrath, D., Steffen, K., Holland, P. R., Scambos, T., Rajaram, H., Abdalati, W., & Rignot, E. (2014). The structure and effect of suture zones in the Larsen C Ice Shelf, Antarctica. *Journal of Geophysical Research: Earth Surface*, *119*(3), 588–602. https://doi.org/10.1002/2013JF002935

McMahon, K. L., & Lackie, M. A. (2006). Seismic reflection studies of the Amery Ice Shelf, East Antarctica: Delineating meteoric and marine ice. *Geophysical Journal International*, *166*(2), 757–766. https://doi.org/10.1111/j.1365-246X.2006.03043.x

Mikucki, J. A., Auken, E., Tulaczyk, S., Virginia, R. A., Schamper, C., Sørensen, K. I., et al. (2015). Deep groundwater and potential subsurface habitats beneath an Antarctic dry valley. *Nature Communications*, *6*(1), 6831. https://doi.org/10.1038/ncomms7831

Miles, K. E., Hubbard, B., Luckman, A., Kulessa, B., Bevan, S., Thompson, S., & Jones, G. (2025). Influence of the grounding zone on the internal structure of ice shelves. *Nature Communications*, *16*(1), 4383. https://doi.org/10.1038/s41467-025-58973-2

Morlighem, M., Rignot, E., Binder, T., Blankenship, D., Drews, R., Eagles, G., et al. (2020). Deep glacial troughs and stabilizing ridges unveiled beneath the margins of the Antarctic ice sheet. *Nature Geoscience*, *13*(2), 132–137. https://doi.org/10.1038/s41561-019-0510-8

Nicholls, K. W., Makinson, K., & Venables, E. J. (2012). Ocean circulation beneath Larsen C Ice Shelf, Antarctica from in situ observations. *Geophysical Research Letters*, *39*(19), L19608. https://doi.org/10.1029/2012GL053187

Perkin, R., & Lewis, E. (1980). The practical salinity scale 1978: Fitting the data. *IEEE Journal of Oceanic Engineering*, *5*(1), 9–16. https://doi.org/10.1109/JOE.1980.1145441

Sharqawy, M. H., Lienhard, J. H., & Zubair, S. M. (2010). Thermophysical properties of seawater: A review of existing correlations and data. *Desalination and Water Treatment*, *16*(1–3), 354–380. https://doi.org/10.5004/dwt.2010.1079

Stubblefield, A. G., Wearing, M. G., & Meyer, C. R. (2023). Linear analysis of ice-shelf topography response to basal melting and freezing. *Proceedings of the Royal Society A*, *479*(2277), 20230290. https://doi.org/10.1098/rspa.2023.0290

Treverrow, A., Warner, R. C., Budd, W. F., & Craven, M. (2010). Meteoric and marine ice crystal orientation fabrics from the Amery Ice Shelf, East Antarctica. *Journal of Glaciology*, *56*(199), 877–890. https://doi.org/10.3189/002214310794457353